EFFECTS OF STREAMWISE VARIATION IN PRESSURE GRADIENT ON TURBULENT BOUNDARY LAYERS

Ashley L. Kwong, Dea D. Wangsawijaya, and Bharath Ganapathisubramani
Department of Aeronautics and Astronautics
University of Southampton
Southampton, SO16 7QF, United Kingdom
A.L.Kwong@soton.ac.uk

ABSTRACT

Turbulent boundary layers under favourable-adverse pressure gradients (FAPG) are of interest given their occurrence in many fundamental engineering flows. In this study, we examine the effect of the streamwise length scale of pressure gradient variation on high Reynolds number turbulent boundary layers ($Re_\tau = U_\tau \delta_0 / \nu \approx$ 6000–8000). Experiments are carried out with a wing of chord $3\delta_0$ (where δ_0 is the incoming boundary layer thickness) mounted in the freestream to generate pressure gradients, following the setup of Preskett *et al.* (2025) where a wing of chord $16\delta_0$ was used. Three cases ranked by the amplitude of $(dC_p/dx)\delta_0$ are presented: Case 2 matches the peak $(dC_p/dx)\delta_0$ of Preskett *et al.* (2025), enabling a direct comparison of pressure gradient length at the same Re_τ, while Cases 1-3 examine the effect of increasing amplitude for the shorter gradient. Results from OFI, PIV, and HWA at $\Delta x/\delta_0 = 3$ downstream show that the streamwise length of the pressure gradient governs the response of C_f and the reorganisation of coherent flow structures, with longer gradients producing more sustained history effects than shorter ones of matched peak amplitude.

INTRODUCTION

Turbulent boundary layers (TBL) subject to pressure gradients are common in engineering applications, including flows over ship hulls and aircraft wings. These pressure gradients perturb the canonical TBL, causing accelerations (favourable pressure gradients, FPG) or decelerations (adverse pressure gradients, APG) of the freestream. In practice, pressure gradients rarely occur in isolation; studying complex sequences such as favourable-to-adverse pressure gradients (FAPG) is therefore directly relevant. FAPGs cause the boundary layer to deviate more rapidly from the canonical log-law relationship, in some cases suppressing the log region entirely and producing an asymmetric recovery — a consequence of upstream conditions affecting the downstream flow, known as pressure gradient history effects Bobke *et al.* (2017). These history effects present significant challenges for modelling; in commercial software, their neglect has led to discrepancies exceeding 10% (Vinuesa *et al.* 2014). In regards to the transportation sector, these numbers have huge implications for the monetary and environmental costs. Though complex pressure gradient history effects have been studied, these studies have been typically focused on weak to moderate pressure gradients, instead of a strong pressure gradients.

In Preskett *et al.* (2025) weak to moderate FAPGs were imposed on a smooth and rough wall turbulent boundary layers for a $Re_\tau \approx 6000 - 8000$. They developed a model for the development of C_f using a linear relationship between a cumulative definition of β, the Clauser pressure gradient parameter and Π, the wake strength parameter. This signified not only the dominance of Π for PG TBLs, but that outer layer characteristics were sufficient to uniquely describe the state of the boundary layer. In these studies, as well as in most studies involving complex pressure gradient sequences (Parthasarathy & Saxton-Fox 2023; Tsuji & Morikawa 1976; Volino 2020), there has been a focus on varying the strength of the pressure gradient imposed, where the length of the pressure gradient imposed was much larger than the largest length scales of the flow. Compared to smaller scales, large-scale motions respond slower to pressure gradients, while transferring momentum between scales, in non-linear coupling further complicating flow dynamics and history effects (Lozier *et al.* 2024). In this study, we focus on the effect of the temporal and spatial duration of pressure gradients by imposing matched and stronger pressure gradients over a shorter streamwise length on the same smooth walled turbulent boundary layer as Preskett *et al.* (2025) and Virgilio *et al.* (2025) at $Re_\tau \approx 6000 - 8000$.

METHODOLOGY

Pressure gradients were generated using a NACA0012 wing with a chord, $c = 0.3$ meters and a trailing-edge flap at $2c/3$. FAPGs were created by putting the wing nose down, with the maximum acceleration occurring under the leading edge of the wing, and maximum deceleration at the trailing edge. The flap allowed for an increase in the strength of the APG, by changing the stagnation point at the trailing edge− similar to Vinuesa *et al.* (2014). We present three cases of the generated FAPG sequences shown in Table 1, where $(dC_p/dx)\delta_0$ is the magnitude of the pressure gradient scaled by the thickness of the ZPG boundary layer at the first measurement position. 126 pressure taps on the floor of the wind tunnel were used to measure the pressure gradient. Pressures were zeroed with respect to the nominal ZPG condition of the tunnel via $(C_p) = (C_p)_{Case} - (C_p)_{ZPG}$.

To compare the effect of pressure gradient length, the peak strength in terms of the amplitude of the $(dC_p/dx)\delta_0$, where δ_0 is the incoming boundary layer thickness obtained with Particle Image Velocimetry, was matched for smooth wall $\alpha = -8$ at $h = 500$ mm from Preskett *et al.* (2025), which we refer to as VP2025. Here we consider values greater than $\Delta dC_p/dx\delta_0$ of 0.03 to be different. Oil Film Interferome-

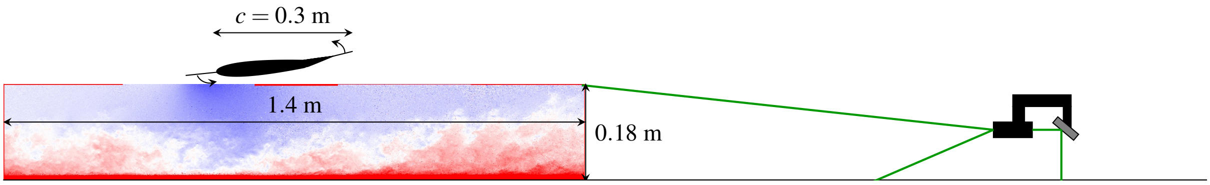

Figure 1. Diagram showing the field-of-view for the Particle Image Velocimetry measurements. A LaVision sheet optic and a mirror were mounted in the tunnel at approximately 1 meter from the trailing edge, with the laser beam coming from the tunnel floor. The blockage of the assembly was $\approx 5\%$ of the tunnel area

try (OFI), Particle Image Velocimetry (PIV) and Hot Wire Anemometry (HWA) were conducted in the Göttingen type Boundary Layer Wind Tunnel at the University of Southampton.All testing was conducted at 18°C.

Oil Film Interferometry

Direct measurements of the wall shear stress, τ_w, were conducted over a length of 2.4 m, capturing $\Delta x/\delta_0 = 4$ upstream from the leading edge and $\Delta x/\delta_0 = 6$ downstream from the trailing edge. OFI was conducted from underneath the tunnel through glass floor panels in the test section, with an average of 165 oil droplets over the 2.4 m span and each measurement repeated twice. A Philips 35 W SOX-E bulb provided a monochromatic light source at a nominal wavelength of 589 nm. Polycraft Dow Corning 200/50 Silicone Fluid was used to generate the fringe patterns; its viscosity was determined at the measurement temperature using a rheometer and a polynomial calibration curve. Images were captured at $f_s = 1$ Hz using five LaVision CMX3-25 CMOS cameras with Nikon 50 mm F2.0 lenses, and the spatial frequency of the fringe patterns was extracted using an FFT-based in-house code.

Planar Particle Image Velocimetry

Planar PIV was conducted over a window of 1.4 by 0.18 meters starting $\Delta x/\delta_0 = 4$ upstream of the leading edge and ending $\Delta x/\delta_0 = 2$ downstream of the trailing edge. The experimental set-up is shown in figure 1. Five LaVision CMX3-25 CMOS cameras with 50 mm Nikon lenses resulted in a resolution of $17.7 : \frac{\text{pixel}}{\text{mm}}$ in the streamwise and wall-normal directions. The light source was a Litron Bernoulli 200-15 Nd:YAG laser emitting 532 nm wavelength. The flow was seeded using a JEM Pro-Fog generator; the resulting particles had an image diameter of approximately 3 pixels. The mean velocity fields and statistics were averaged over 2000 images taken at a sample rate of $f_s = 2$ Hz. This was done such that the number of boundary layer turnovers $N_{turnovers} = \frac{N_{images} U_\infty}{f_s \delta_0}$ $> 19,000$, ensuring statistical convergence of the first order mean quantities. Image pairs were processed using an in-house code for the cross-correlation. Five passes of correlation windows were used: 16×96, 16×48, 8×32 and two passes of 8×24 with overlaps of 50%, 50%, 50%, 75%, 75% respectively. The asymmetric window was optimized for the boundary layer flow presented here. This gave a final resolution of 0.36 mm per window in the streamwise and 0.1 mm per window in the wall-normal. The $\Delta t = 49.6, \mu$s was chosen such that the average pixel displacement in the boundary layer was 10 pixels on average for a $U_\infty = 20$,m/s, in accordance with Raffel *et al.* (2018). The freestream velocity was set using a Pitot tube positioned 1.2 m upstream of the aerofoil leading edge. The dynamic pressure was recorded using a Furness FCO560 micromanometer with a PT100 probe to monitor the temperature.

Hot Wire Anemometry

Hot-wire anemometry measurements were conducted at two downstream distances from the trailing edge. Here, we present results from the first downstream station at $\Delta x/\delta_0 = 3$, which lies within the PIV window, enabling comparison of the mean velocity and turbulence intensity profiles with the two-point spatial correlations from PIV. HWA was conducted using an in-house repaired Dantec 55P05 single wire probe and a Dantec Dynamics Streamline Pro system in constant temperature mode. The probe consists of a 5 μm diameter tungsten wire with a sensing length of 1 mm, giving a length-to-diameter ratio of 200, satisfying the criterion of $l/d \geq 200$. The overheat ratio was set to 0.8. The signal was acquired at $f_s = 60$ kHz using an NI USB-6212 16-bit DAQ; square wave testing confirmed adequate frequency response, and a low-pass filter was applied at 30 kHz. A traverse with a fairing was mounted behind the wing and had an optical encoder with a resolution of 1μ m. The wire's initial wall-normal position was set using a microscope camera. A second Pitot tube was mounted on the traverse, level with the probe to allow for calibration. Calibrations were taken before and after each measurement and the temperature drift was found to be within 2% between runs. A fourth order polynomial with temperature correction was used to convert the voltages to velocities. The data was sampled such that $TU/\delta_{99} \geq 20,000$.

RESULTS

Pressure Gradient Histories

Figure 2a presents $(dC_p/dx)\delta_0$ as a function of $\Delta x/L_{PG}$, where L_{PG} is the pressure gradient length determined from pressure tap readings. Here, the start of the pressure gradient is defined as $\Delta x/L_{PG} = 0$. In Preskett *et al.* (2025), the wing chord length was $\approx 15.6\delta_0$, with the length of pressure gradient extending $48.2\delta_0$. In contrast, the pressure gradients generated in cases one through three have a wing and pressure gradient length that extend $\approx 3\delta_0$ and $\approx 16.6\delta_0$ respectively. Case 2 matches the peak amplitude of the $\frac{dC_p}{dx}\delta_0$, in both the FPG and APG regions, allowing for the study of the effect of pressure gradient length on high Reynolds number turbulent boundary layers. In the following sections, an examination of the response of the C_f will be followed by the two point spatial correlation of the streamwise fluctuations will be examined between the two cases for three stations marked in $(--)$ on Figure 2a. The effect of increasing pressure gradient strength, the peak value of $(dC_p/dx)\delta_0$, is then examined for the short pressure gradient cases. Mean velocity profiles and streamwise Reynolds normal stress, $\overline{u'^2}$, are compared against the zero-pressure-gradient condition. All quantities scaled by the friction velocity, $U_\tau = \sqrt{\tau_w/\rho}$, are denoted with superscript $^+$

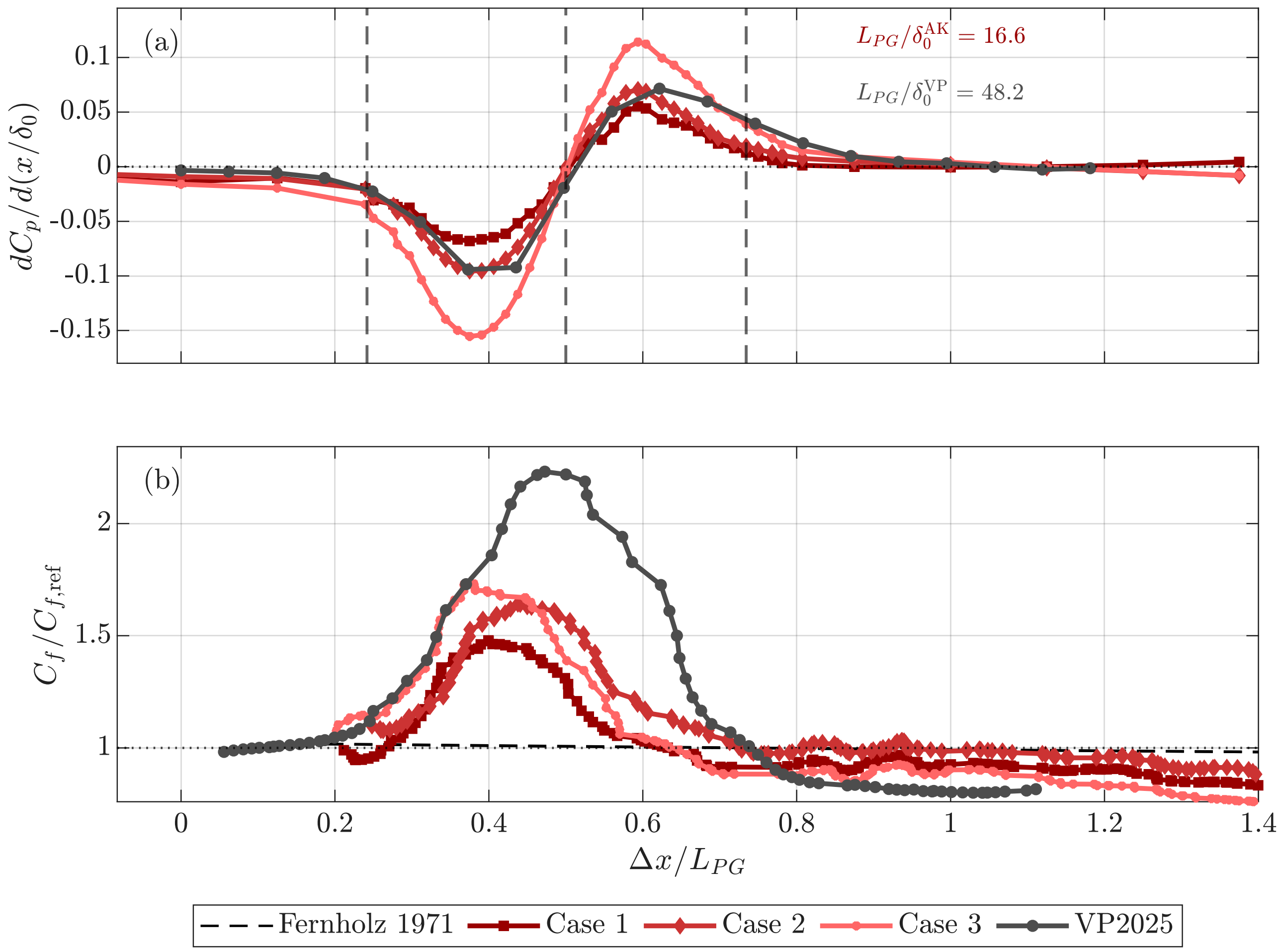

Figure 2. $(dC_p/dx)\delta_0$ (a) and $C_f/C_{f,ref}$ (b) vs $\Delta x/L_{PG}$. For the same matched peak $(dC_p/dx)\delta_0$, VP2025 exhibits a greater peak $C_f/C_{f,ref}$ and a persistent undershoot in the recovery region compared to Case 2.

Development of C_f

The skin friction coefficient is defined as $C_f = 2\tau_w/(\rho U_\infty^2)$, where U_∞ is the freestream velocity measured from PIV in the ZPG region downstream of the wing, chosen to account for the upstream blockage effects of both wings. The C_f for each case is normalised by the ZPG value at the start of the pressure gradient, $C_{f,ref}$. Figure 2b shows that VP2025 exhibits a greater amplification in C_f than Case 2. Furthermore, in the recovery region ($\Delta x/L_{PG} > 1$), VP2025 exhibits a persistent undershoot relative to the Fernholz correlation for the local Re_x, whereas the shorter pressure gradient case recovers more closely to the canonical ZPG value. This behaviour highlights the importance of pressure gradient length on C_f: as the boundary layer is exposed to the pressure gradient over a greater number of δ_0, it accumulates more history, and the resulting departure from equilibrium is more sustained. This is consistent with Virgilio *et al.* (2025), who demonstrated that shorter spatially varying pressure gradients affect only a limited portion of the TBL evolution, while longer-lasting ones produce more persistent effects.

Two Point Correlation

Two-point spatial correlations were computed as

$$R(r) = \frac{\overline{u_1' u_2'}}{\sqrt{\overline{u_1'^2}} \cdot \sqrt{\overline{u_2'^2}}} \qquad (1)$$

Three streamwise reference locations are selected, highlighted in Figure 2a, representing the inlet, the midpoint where the pressure gradient changes sign, and the recovery region, for $y_{ref}/\delta = 0.05$ and $y_{ref}/\delta = 0.5$. Contour levels of $R = 0.3$ and $R = 0.6$ are presented to examine the response of large- and small-scale structures to the different pressure gradient lengths. FPGs are known to elongate structures and reduce the inclination angle, while APGs have the opposite effect (Harun *et al.* (2013)). Figure 3 reveals that at matched $(dC_p/dx)\delta_0$ values, the structures in VP2025 undergo substantially greater changes than those in Case 2. In the log region, clear FPG-driven elongation is visible in VP2025 (Figure 3b), while in the recovery region the APG-induced reduction in streamwise correlation length persists. In contrast, the structures of Case 2 show little change in either extent or inclination throughout the domain, demonstrating that the short pressure gradient is insufficient to produce lasting structural modification.

The persistence of structural change in VP2025 explains the sustained C_f deficit in the recovery region. Changes in large-scale structure are known to modulate near-wall scales through amplitude modulation (Harun *et al.* (2013)), so the greater structural modification in VP2025 translates directly to a larger and more sustained departure of C_f from equilibrium. This is consistent with (Virgilio *et al.* (2025)), who demonstrated that longer pressure gradients accumulate flow history progressively, producing effects that persist well into the recovery region.

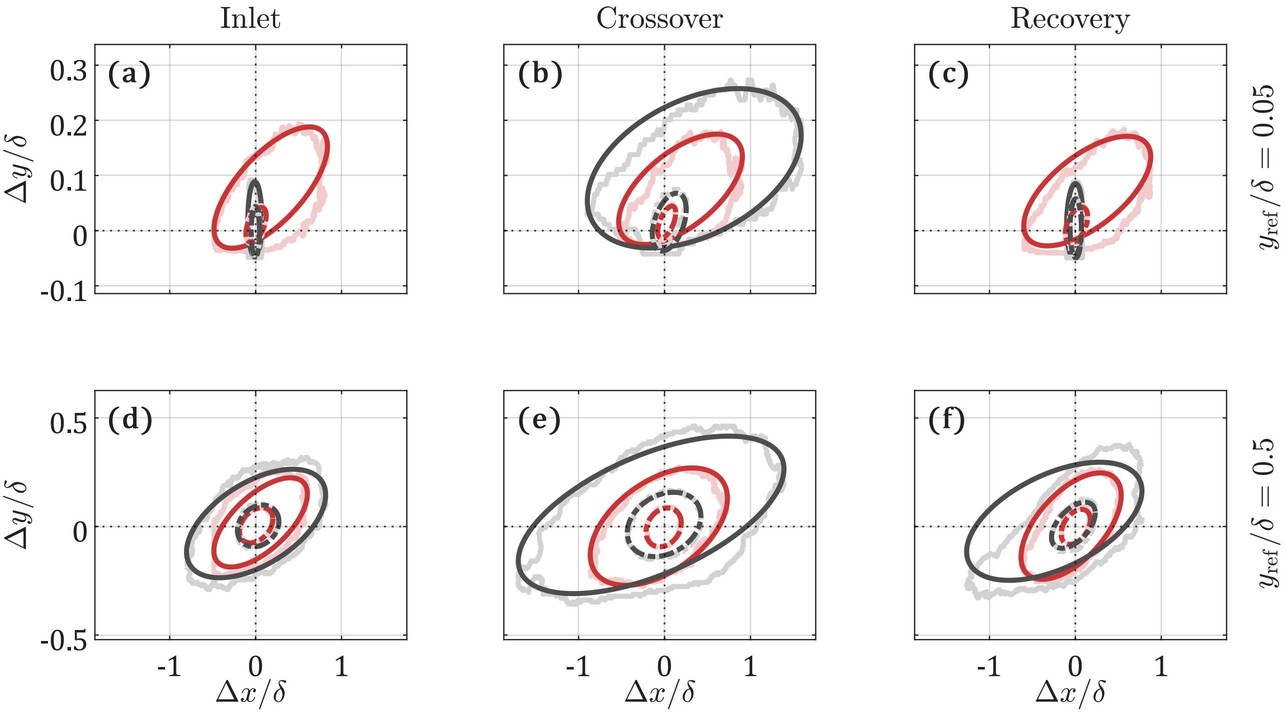

Figure 3. $R_{u'u'}$ contours with elliptical fits for $R = 0.3$ (—) and $R = 0.6$ (– –) comparing Case 2 and VP2025 at matched $(dC_p/dx)\delta_0$. Figures 3(a–c): log region, $y_{\mathrm{ref}}/\delta = 0.05$; Figures 3(d–f): wake region, $y_{\mathrm{ref}}/\delta = 0.5$.

Increasing $\frac{dCp}{dx}\delta_0$ for a Short Spatial Pressure Gradient

The response of the TBL to increasing pressure gradient amplitude is now examined. The two-point spatial correlations of Cases 1–3 show no significant differences in structure size or inclination across the range of amplitudes tested. Figure 4 presents mean velocity and turbulence intensity profiles for Cases 1–3 compared against the ZPG reference, in both inner and outer scaling. The mean profiles show a lack of a well-developed wake region, which would be expected after a longer APG history, consistent with the short pressure gradient length of the cases presented here. The turbulence intensity profiles, however, do show characteristic energisation of the large-scale motions, suggesting that while the pressure gradient increases the energy content of the structures, it does not alter their spatial organisation.

This is further confirmed in Figure 5, which presents two-point spatial correlations at $y_{\mathrm{ref}}/\delta = 0.05$ and 0.5 in the recovery region for contour levels of $R = 0.3$ and $R = 0.6$. Across all cases, both wall-normal locations show a lack of variation in structural size and inclination. Thus, while increasing pressure gradient amplitude increases the energy imparted to the structures, it does not reorganise them — highlighting the importance of δ_0 accumulation rather than peak amplitude in driving lasting structural change.

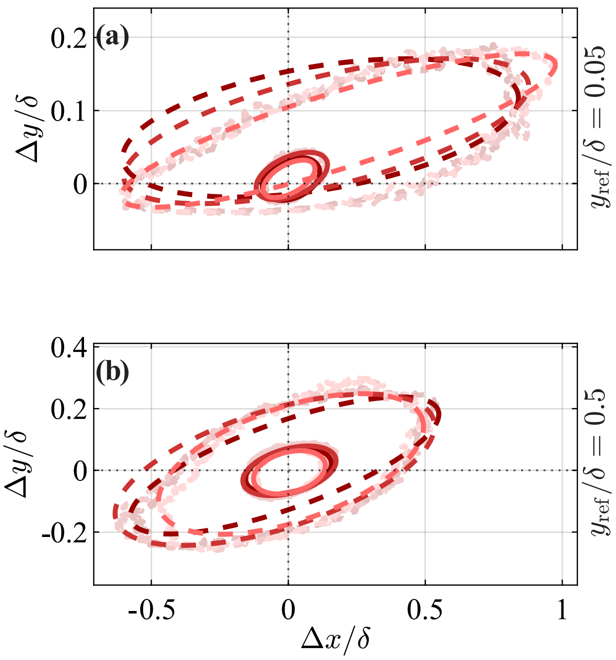

Figure 5. $R_{u'u'}$ contours for $R = 0.3$ (—) and $R = 0.6$ (– –) for Cases 1–3 in the recovery region at $y_{\mathrm{ref}}/\delta = 0.05$ and 0.5.

CONCLUSION

Results from PIV, OFI, and HWA measurements compare the response of a turbulent boundary layer to two pressure gradients of differing spatial extent but matched peak amplitude $(dC_p/dx)\delta_0$. The longer pressure gradient, with $x_{LPG} = 48.6\delta_0$ (VP2025), is compared against the short pressure gradient of $x_{LPG} = 16.6\delta_0$ (Cases 1–3) in the same facility. The development of C_f, normalised by the respective ZPG value, shows that the longer pressure gradient produces

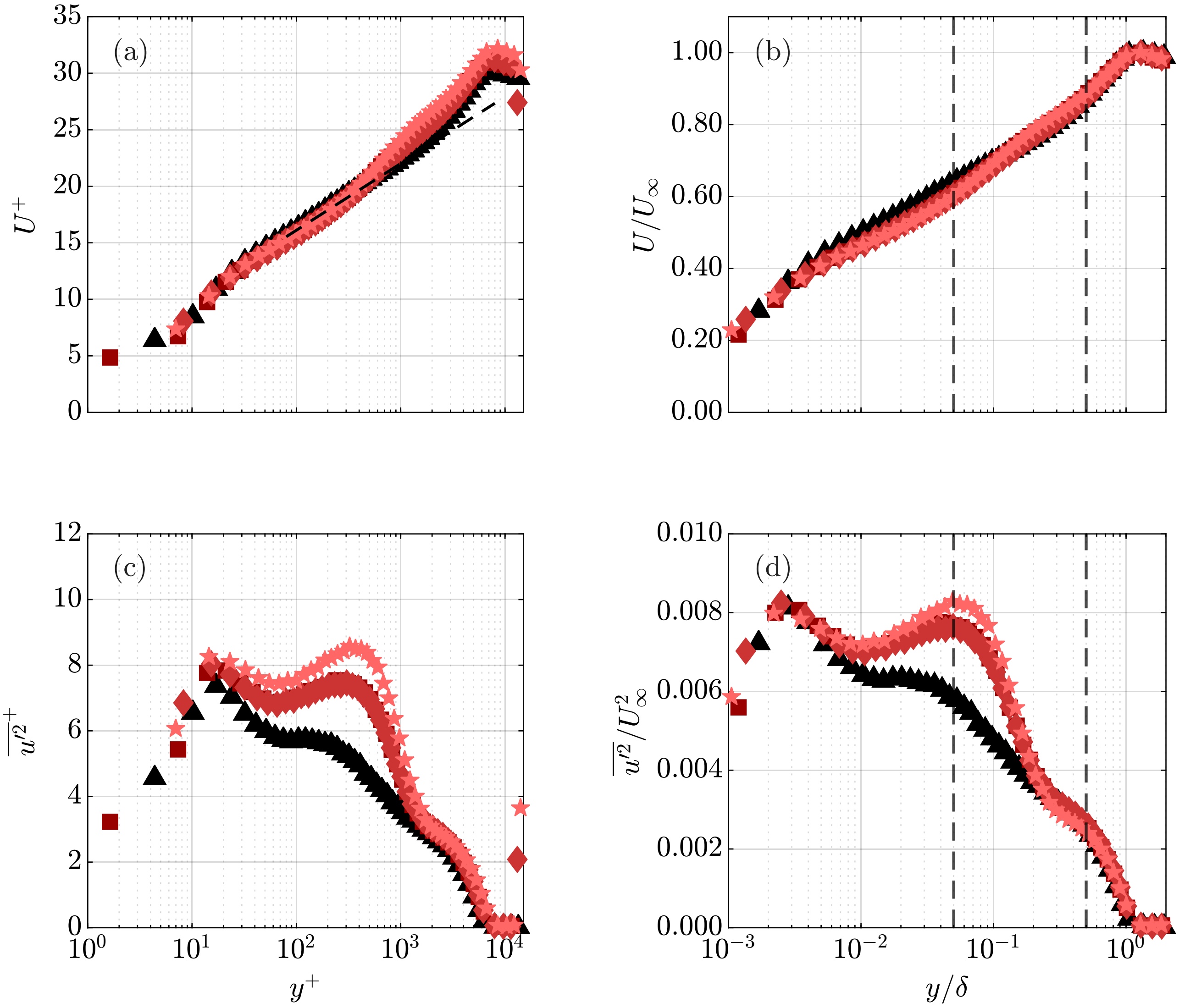

Figure 4. Mean velocity and streamwise Reynolds normal stress $\overline{u'^2}$ profiles for Cases 1–3 compared against the ZPG reference in inner (a-c) and outer scaling (b-d), measured at $\Delta x/\delta_0 = 3$. The dashed lines represent the y_{ref} locations for the two point correlation.

a greater amplification of C_f under the FPG, as the flow is exposed to the favourable gradient over a greater streamwise extent. Correspondingly, the APG-induced reduction in C_f for VP2025 persists beyond the available measurement window, with VP2025 exhibiting a sustained undershoot relative to the Fernholz correlation for the local Re_x. In contrast, the short pressure gradient produces a smaller increase in C_f and recovers more rapidly to the canonical ZPG value, indicating that the duration of exposure — measured in δ_0 — governs the persistence of history effects on C_f. Two-point spatial correlations of the streamwise fluctuations, examined at $y_{\mathrm{ref}}/\delta = 0.05$ and 0.5 for contour levels $R = 0.3$ and $R = 0.6$, reveal the structural origin of this behaviour. The large-scale structures of Case 2 pass through the short pressure gradient relatively unchanged in both length and inclination angle. In contrast, VP2025 shows clear FPG-driven elongation followed by APG-induced reduction in streamwise correlation length, with these modifications persisting into the recovery region. The accumulation of pressure gradient history forces the structures to progressively reorganise, and this reorganisation is retained — directly manifesting in the sustained C_f response. For the short pressure gradient, increasing the peak amplitude $(dC_p/dx)\delta_0$ across Cases 1–3 energises the flow structures, as evidenced by elevated streamwise turbulence intensity in both the log and wake regions from HWA measurements in the recovery region. However, the two-point spatial correlations show no significant change in structural size or inclination across Cases 1–3. This distinction between energisation and structural reorganisation confirms that peak amplitude alone is insufficient to produce lasting structural change — it is the accumulation of pressure gradient history over many δ_0 that drives structural modification and the associated history effects on C_f. Furthermore, the absence of collapse when scaling in δ_0 suggests that δ_0 alone is not the appropriate similarity parameter for flows under varying pressure gradient length; an alternative scaling accounting for the full history of the pressure gradient is required.

REFERENCES

Bobke, A., Vinuesa, R., Örlü, R. & Schlatter, P. 2017 History effects and near equilibrium in adverse-pressure-gradient turbulent boundary layers. *Journal of Fluid Mechanics* **820**.

Harun, Zambri, Monty, Jason P., Mathis, Romain & Marusic, Ivan 2013 Pressure gradient effects on the large-scale structure of turbulent boundary layers. *Journal of Fluid Mechanics* **715**.

Lozier, Mitchell, Marusic, Ivan & Deshpande, Rahul 2024 Revisiting amplitude modulation in non-canonical wall-turbulence through high-Reynolds number experimental data. *Physical Review Fluids* **9**.

Parthasarathy, Aadhy & Saxton-Fox, Theresa 2023 A family of adverse pressure gradient turbulent boundary layers with upstream favourable pressure gradients. *Journal of Fluid Mechanics* **966**.

Preskett, T, Virgilio, M, Jaiswal, P & Ganapathisubramani, B 2025 Effects of pressure-gradient histories on skin friction and mean flow of high Reynolds number turbulent boundary layers over smooth and rough walls. *Journal of Fluid Mechanics* **1010**, A30.

Raffel, Markus, Willert, Christian E, Scarano, Fulvio, Kähler, Christian J, Wereley, Steven T & Kompenhans, Jürgen 2018 Particle Image Velocimetry: A Practical Guide. *Particle Image Velocimetry: A Practical Guide* .

Tsuji, Yutaka & Morikawa, Yoshinobu 1976 TURBULENT BOUNDARY LAYER WITH PRESSURE GRADIENT ALTERNATING IN SIGN. *Aeronaut Q* **27** (pt 1).

Vinuesa, Ricardo, Rozier, Paul H., Schlatter, Philipp & Nagib, Hassan M. 2014 Experiments and computations of localized pressure gradients with different history effects. *AIAA Journal* **52** (2).

Virgilio, Marco, Preskett, Thomas David, Jaiswal, Prateek & Ganapathisubramani, Bharath 2025 Pressure gradient history effects on integral quantities of turbulent boundary layers: Experiments and data-driven models. *Tech. Rep.*.

Volino, Ralph J. 2020 Non-equilibrium development in turbulent boundary layers with changing pressure gradients. *Journal of Fluid Mechanics* **897**.